Supplementary Material

S.1. Experimental Setup

S.1.1. Faraday Cage Assembly

To obtain conditions with electric fields sufficiently small to allow the ions produced by REMPI to drift nearly free of any external field, a Faraday cage assembly of rectangular parallelepiped form was constructed from tungsten meshes (Advent Research Materials Ltd, Oxford, England, 99.95% transmission, 0.025 mm thick wires). Patch fields were minimized by spray coating the tungsten mesh with colloidal graphite (CRC Industries Europe, Graphit 33) to form a graphite layer.

A drawing of the assembly is shown in Figure S 1, with a perspective view in panel (b) and a cross section in panel (a), where the parts are indicated by numbers. Two aluminum frames (grey in panel b) fixed all parts and were separated by rods (aluminum, dark grey) to set the length of the assembly (102 mm) along the laser direction. On these frames metal rods (WCu-alloy, 75%W, brown in panel (b), number 1 in panel (a)) were fixed, electrically insulated from the frame. These rods held a single mesh (~105 mm x ~60 mm, number 2 in panel (a) and green in panel (b)) to construct four sides of the Faraday cage, which allowed for resistive heating (~6-7 W) to avoid adsorption of molecules like water or hydrocarbons on the mesh; the heating current was switched off 300 µs before the laser pulse and back on 150 µs after laser the laser pulse, a sufficiently long time that all ions left the drift region before the heating was turn back on. The heating proved necessary to prevent adsorption of molecules on the mesh, which could create patch fields due to their different work functions or by charging. The two open ends of the assembly were closed by additional meshes on separate frames (light blue in panel (b), ~30 mm x ~30 mm, 4 mm holes for laser entry and exit). The total dimensions of the faraday cage in this assembly were: 32.5 mm in drift direction, 60 mm along laser propagation direction and a width of 20 mm. Ions generated inside had a view only of the meshes and holding rods, not to the supporting frame. An additional heated mesh (number 4 in panel (a), 43 mm x 53 mm) on top of the faraday cage assembly further shielded it from the ion optics, elongating the drift region and improving the shielding in the direction perpendicular to the laser beam.

The ion optics consisted of two metal tubes held at attractive potentials. The first tube was equipped with a mesh parallel to the shielding mesh, to extract the ions with a homogenous field. The second tube was held at higher potential to accelerate and focus the particles onto the micro channel plate (MCP, Scientific Instruments GmbH, Gilching, Germany, Chevron setup) detector. The electrical signal was pre-amplified and ion pulses counted by a multi-channel scaler (EG&G Ortec, Turbo MCS).

The drift length inside the field free region was sufficiently long (~29 mm) to allow for resolving the energy distributions. During acquisition, the number of ions generated by each laser pulse was low enough to prevent space charge from significantly influencing the energy of the ions in the faraday cage.

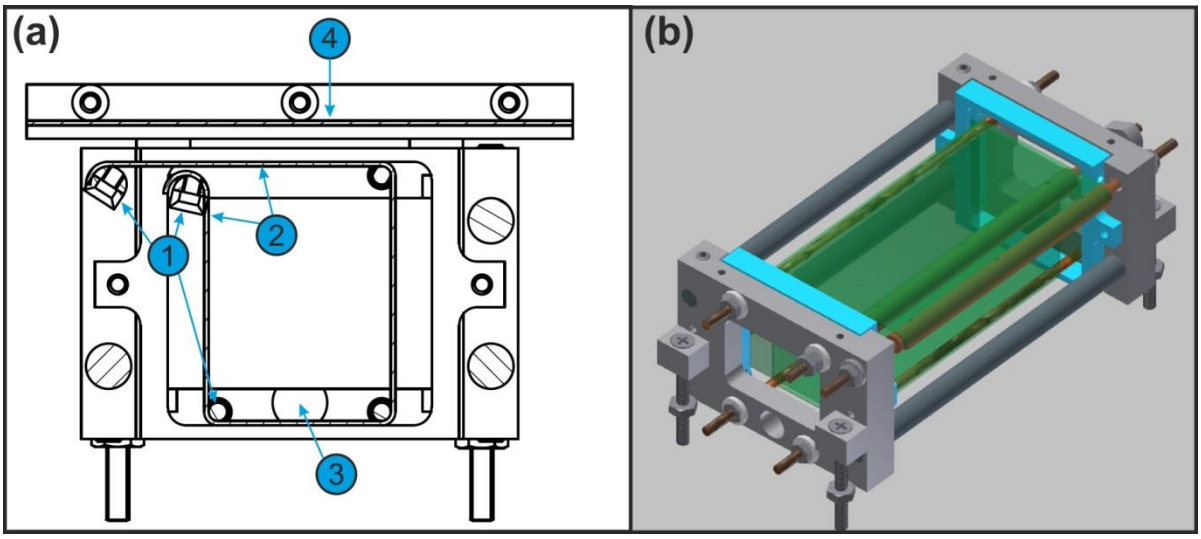

Figure S 1: Drawings of the faraday cage assembly. Panel (a) gives a cross-section including indicators for the important parts: Marked with (1) are the metal rods fixing and forming the long mesh (2) into a cage. The ionization spot is marked with (3), and the ions have to pass through the initial cage as well as an additional shielding mesh (4) mounted on top of the assembly. Shown in panel (b) is a perspective view of the assembly, with the meshes in green and the metal rods in brown. An aluminum frame (grey) fixed all parts and the length of the cage was adjusted by separate rods (dark grey).

S.1.2. Laser system

The Hydrogen molecules were detected quantum state resolved by resonantly enhanced multi photon ionization (REMPI). The (2+1) REMPI scheme used here utilizes a two photon transition to the *E,F* $^1\Sigma_g^+$ state in the range 201-215 nm[1]. The laser system generating this radiation consisted of a Nd:YAG laser (Continuum, Powerlite 8050, 50 Hz, ~7 ns) and a dye laser (Sirah, Precision Scan). The output of the YAG laser was frequency doubled to 532 nm and used to pump the laser dye. Depending on the wavelength range needed the dye was either DCM (Radiant Dyes) in ethanol or a mixture of Rhodamines B and 101 (Lambda Physik) in ethanol. The radiation of the dye was successively frequency doubled and then mixed with the doubled light to yield the needed range of 201-215 nm with a pulse power of ~1 mJ. This light was focused into the UHV chamber by a plano-convex lens of ~205 mm focal length at 201-215 nm (UV fused silica, uncoated, Thorlabs).

S.1.3. Permeation Sources

The permeation sources (MaTeck Material-Technologie & Kristalle GmbH, Juelich, Germany, 99.999% purity) consisted of cylindrical copper single crystals, 8 mm long and with a diameter of 8 mm. The surface facets in this investigation were (111) and (211), both polished to an accuracy of <0.1°. These samples were machined using electrical discharge machining from the backside to form a hollow channel of 3 mm diameter, leaving a ~0.3 mm thick membrane at the front. This crystal was brazed with copper onto a stainless steel support tube, which allowed mounting to the sample holder and gas supply.

The crystals were surrounded by a cylindrical heater assembly made of a Boron Nitride body holding a coil of Tantalum wire (Goodfellow, 0.25 mm diameter). This was resistively heated, transferring the heat to the sample by conduction and radiation. The sample temperature was measured by a type K thermocouple, which was stuck firmly into a small indent of the crystal.

The Cu(111) (Cu(211)) crystals were cleaned by Ar^+-ion sputtering for 30 (20) minutes and successive annealing at 500°C (450°C) for 20 minutes. The absence of contaminants was checked by Auger electron spectroscopy and the surface structure by low energy electron diffraction (LEED). After several hours of permeation, the amount of carbon on the surface rose to detectable amounts and the

crystal was cleaned again. The rate of contamination decreased with ongoing experiments, due to the depletion of carbon from the bulk. It should be noted that the shape of the TOF distributions did not change within experimental accuracy despite variations in the carbon contamination levels over up to 19%. Despite this, for all the data reported here the carbon contamination was always less than 10% of a monolayer during experiments. Generally, the experiments were started with a contamination level close to the detection threshold of a few percent and rose up to ~5% during several hours of experiment.

LEED patterns have also been determined at permeation temperatures, resulting in a blurred pattern for Cu(111), resulting from thermal motion of the atoms. For Cu(211), the whole pattern blurs rapidly with increasing temperature, and vanishes above ~700K.

Permeation was induced by supplying 1 bar of hydrogen (H_2: Westfalen Gas, 5.0 / D_2: Sigma Aldrich, 99.96 atom % D / HD: 2:1 mixture of D_2:H_2) to the backside of the crystals and heating to temperatures above ~700 K. If not indicated otherwise, the temperature used for all the results presented in this work was (923±3) K, which is a compromise between significant hydrogen flux to acquire, the needed mechanical stability of the crystal at high temperatures, and comparability to literature values.

S.1.4. Knudsen cell

We used a Knudsen cell to produce beams with a Maxwell-Boltzmann velocity distribution for velocity calibration of the experiment. The Knudsen cell consisted of a hollow copper cylinder capped with a molybdenum aperture (Plano GmbH). This aperture had a thickness of 125 µm and a 300 µm diameter diverging 90° conical hole, which was used to avoid channeling effects. The gas supply tube inside the copper cylinder was aligned perpendicular to the main aperture to ensure no molecules could escape without collisions with the wall of the Knudsen cell. The Knudsen source was mounted to the same manipulator used for the permeation source and gas supply and heater assembly like that used for the permeation source. For calibration purposes, hydrogen and deuterium was supplied sequentially to the Knudsen cell at several temperatures, in the range of 300-835K.

S.2. Experimental Methods

S.2.1. Calibration

The signal from the effusive flux of the Knudsen cell was measured as function of TOF and with a density-dependent ionization technique. Therefore, the measured signal is given as[2, 3]:

$$P\left(T_{Kn}, t, x_0, t_{shift}\right) \propto \left(\frac{x_0}{t-t_{shift}}\right)^4 \times \exp\left(\frac{-m}{2k_b \times T_{Kn}}\left[\frac{x_0}{t-t_{shift}}\right]^2\right) \times \text{Cutoff}(E_{kin})\, dt, \quad \text{(S 1)}$$

with the Boltzmann constant, k_b, the Knudsen cell temperature, T_{Kn}, the mass of the molecule, m, and the cutoff function from Eq. (1). The kinetic energy, E_{kin}, is expressed in TOF as:

$$E_{kin}(t) = \frac{m}{2}\left(\frac{x_0}{t - t_{shift}}\right)^2. \quad \text{(S 2)}$$

Figure S 2 gives examples of calibration distributions of H_2 and D_2 in TOF and kinetic energy as well as the resulting cutoff functions. Figure S 3 compares the obtained cutoff function of Figure S 2 to the literature [3, 4] and another cutoff which represents the worst conditions under which we still acquired data. This demonstrates that those effects are only relevant for ions with kinetic energies below 0.1 eV.

It is pointed out, that the drift length (x_0) is different for each Faraday cage assembly and also varies daily due to the laser alignment. While for different setups x_0 can vary by several mm, the day-to-day variations are only on the order of <0.5 mm.

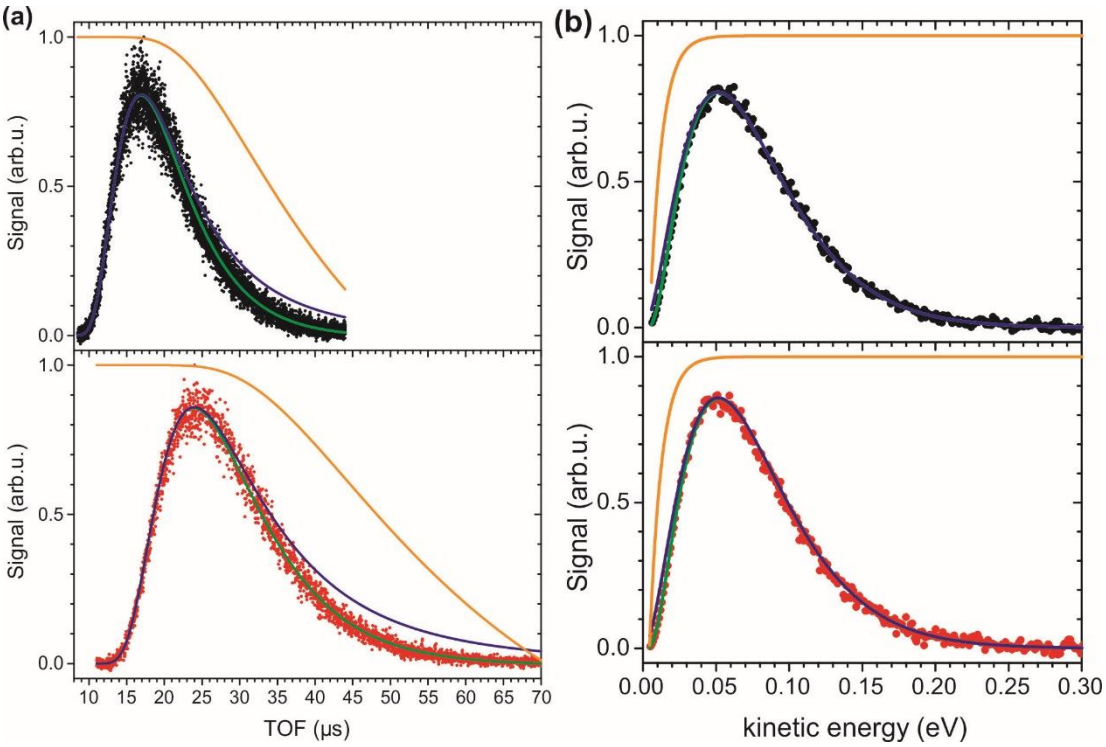

Figure S 2: Typical Knudsen cell traces at 298K used for calibration and comparison to the expected effusive TOF distributions. The left panels show measured TOF distributions of H_2 (black dots) and D_2 (red dots) at room temperature and the corresponding fits (green line) as well as the global cutoff function obtained (brown line). A hypothetical, unaffected effusion distribution is given by the blue lines. The right hand panels show the same datasets converted to kinetic energy scale. The obtained parameters are $\boldsymbol{E_{Min} = 4.4}$ meV and $\boldsymbol{E_{Slope} = 122.8}$ eV^{-1} for the cutoff function and $\boldsymbol{x_0 = 30.5}$ mm for the drift length.

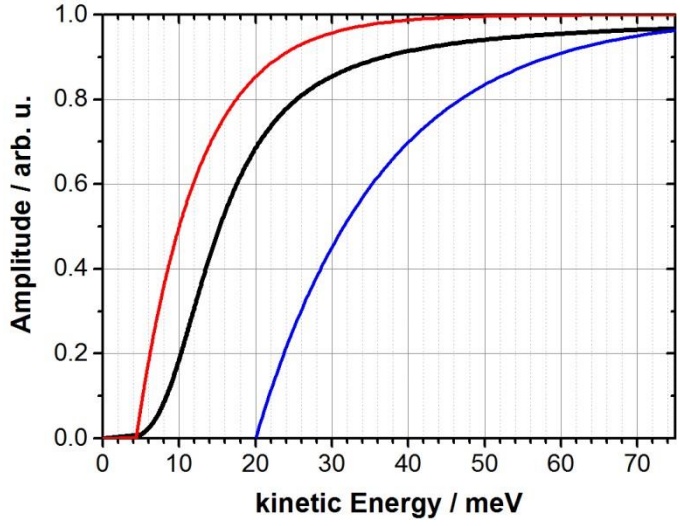

Figure S 3: More detailed view of the exponential-function based cutoff function in Figure S 2 (red), compared to the tanh-function reported in the literature (black)[3, 4]. Additionally given as blue line is the exponential-function with the parameters $\boldsymbol{E_{Min} = 20}$ meV and $\boldsymbol{E_{Slope} = 60}$ eV^{-1}, which corresponds to the worst cutoff conditions under which data was acquired.

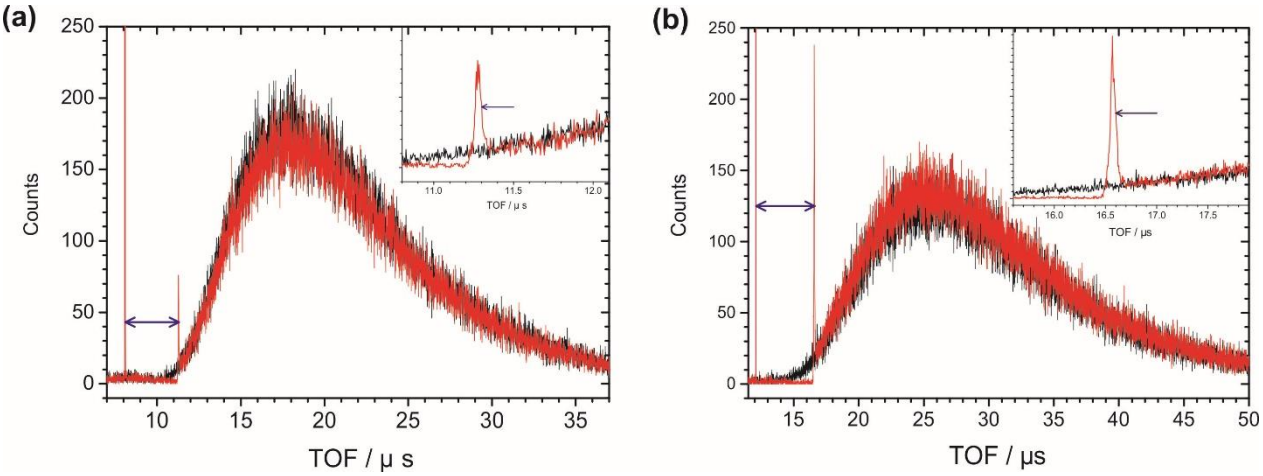

Figure S 4: Results of the extraction switching experiment described in Section 3.1, for H_2 and D_2 in panels (a) and (b). Black lines indicate undisturbed TOF distributions and red lines with switching. The insets show enlarged Sections of the TOF distributions and blue arrows indicate the data points used to determine the $\boldsymbol{t_{shift}}$.The blue double arrows show the TOF delay between the electrical noise of the voltage switch and the initial peak of the ion distributions.

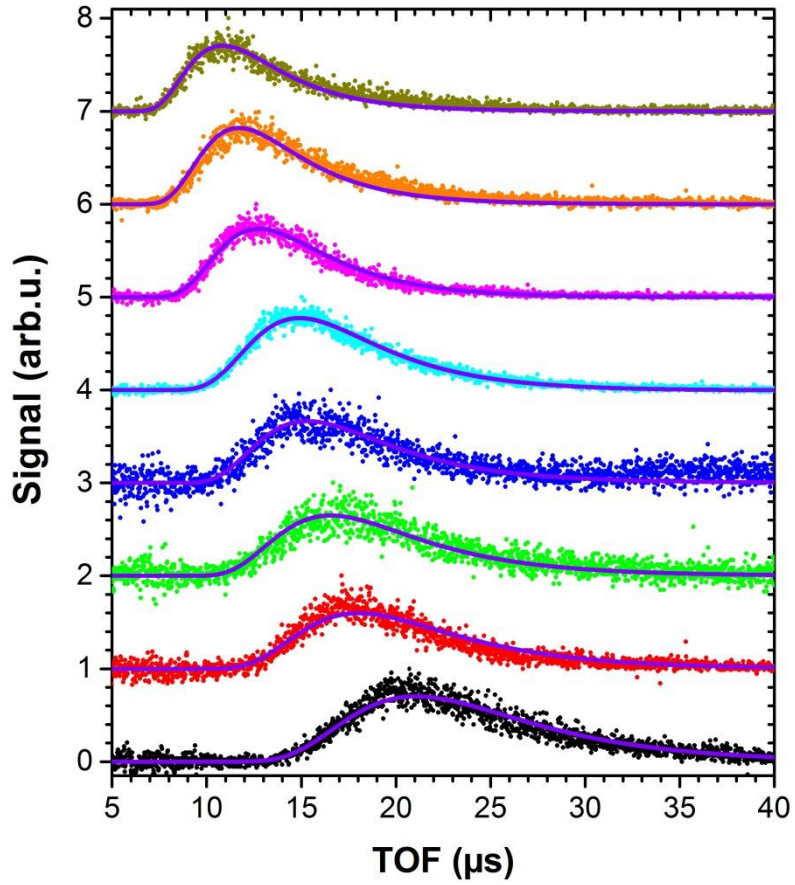

Figure S 5: Illustrative calibration data set, with each TOF distribution normalized and offset on the vertical axis. The traces show D_2 (black, red, green, dark blue) and H_2 (light blue, pink, orange, brown) for the temperatures 299 K, 490 K, 648 K and 835 K, respectively. The global model determined by fitting is shown as purple lines and results in the following parameters: $\boldsymbol{x_0 = 29.25 \pm 0.09}$ mm, $\boldsymbol{t_{shift}^{H_2} = 3.2 \pm 0.1}$ µs, $\boldsymbol{E_{Min} = 7.2 \pm 0.3}$ meV and $\boldsymbol{E_{Slope} = 22.8 \pm 0.9}$ eV^{-1}.

S.2.2. Cutoff Conditions

In order to demonstrate the impact of cutoff function on the desorption signals, Figure S 6 shows two TOF distributions for H_2/Cu(211) (v=1, J=1), both at a temperature of 1023 K and acquired within a

few hours. Thus, it is assumed that the calibration parameters ($x_0 = 28.93$ mm and $t_{shift}^{H_2} = 3.2$ µs) did not change significantly.

Here, the signal (black dots), model fit (red line) and the cutoff function (blue line, right hand scale) are given. In panel (a) the cutoff was almost negligible and both channels are clearly discerned. Apparently, the cutoff does not rely on data points with significant amplitude and the obtained values ($E_{Min} = 4.13$ meV and $E_{slope} = 2232$ eV^{-1}) are not well determined. The actual values do not affect the analysis as long as the cutoff function does not affect data at TOF <35 µs. In contrast to that, panel (b) shows the measurement after the faraday cage assembly was overheated, resulting in distortions and suppression of the slow channel, while the fast channel is almost undisturbed. Here the parameters of the cutoff function are $E_{min} = 23.59$ meV and $E_{slope} = 62.7$ eV^{-1}, outside the range of the values used in this study.

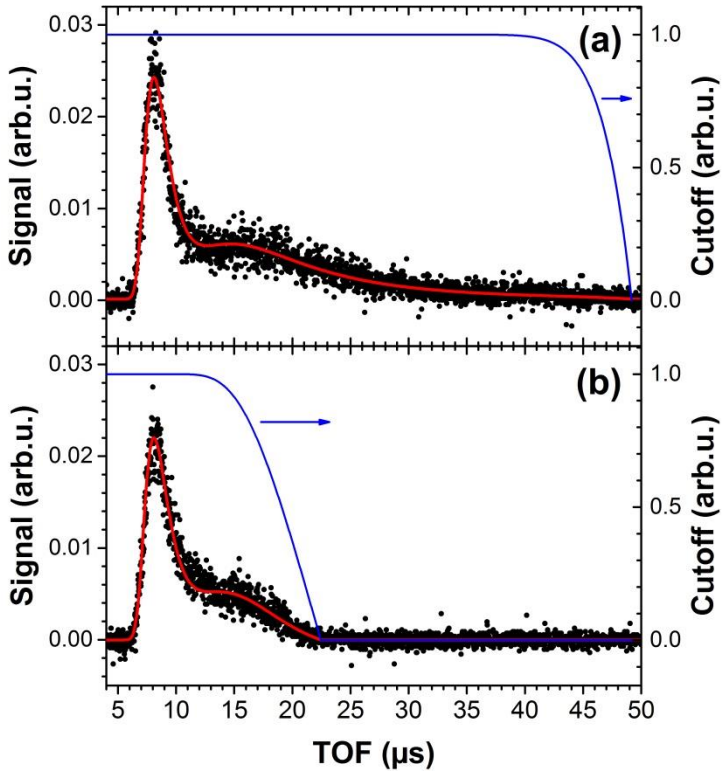

Figure S 6: Influence of faraday cage properties on desorption peaks. Both panels show data from Cu(211), H_2 (v=1, J=1) desorbing at 1023 K. The TOF data is shown as black dots, the obtained fit as red line and the applied cutoff function as blue line corresponding to the right hand ordinate. In panel (b) Faraday cage assembly had been overheated, destroying the coating on the tungsten meshes. This resulted in more restrictive conditions for the ion drift, which clearly affect the slow reaction channel significantly and suppress its detection, but not the fast channel.

S.2.3. Data Processing and Fitting

Each TOF distribution was corrected for background by subtracting a TOF spectrum measured under identical conditions with the laser wavelength shifted off resonance. This removed most of the scattered light and other minor contributions of background gas, which was ionized by the scattered UV radiation.

The TOF data was analyzed with a Python program, utilizing the Levenberg-Marquardt[5, 6] algorithm implemented in the "lmfit" package[7]. The calibration measurements have been analyzed with the

model in Eq. (4) for x_0 and the cutoff-function parameters E_{Slope} and E_{Min} (Eq.(1)), using a fixed t_{shift} value (Eq.(2)). These calibration parameters were fixed for the analysis of the permeation datasets acquired on the same day.

For analysis of desorption data, the model in Eqs. (4)-(6) was applied and fitted for the parameters of both sticking function contributions. The experimental data was prepared by subtraction of the thermal background and then converted to sticking probability curves using Eq. (7). For the fit, the $\log_{10}$ of the $S(v,J,E_{kin})$ results was used in order to consider the whole dynamic range of the sticking probability.

For the error function, the parameters $A(v,J)$, $E_0(v,J)$ and $W(v,J)$ were fitted. Here, the $W(v,J)$ parameter has been fitted as global variable for data in the same vibrational state, $W(v)$. This constraint improved the reliability for datasets with low signal to noise, while not degrading the fit quality. The $A(v,J)$ result was successively used to re-scale $C(v,J)$ of Eq. (7) to achieve $A(v,J)=1$. The sticking contribution of the slow channel (Eq. (6)) was fitted for the two parameters, $A_{slow}(v,J)$ as the Amplitude in the zero kinetic energy limit and $\gamma_{slow}(v,J)$, the $1/e$-width of the curve.

S.2.4. Thermal Background Subtraction

The TOF distribution of the thermal background has been determined by leaking gas into the detection chamber and pumping away the permeating gas under otherwise identical conditions as during permeation experiments. To simulate the obtained TOF distributions, we start with a Maxwell-Boltzmann velocity distribution at 300 K. But the geometry is different from the Knudsen cell measurements, since the background gas is not ionized from a directed flow restricted by apertures. Background gas is rather ionized along the whole laser focus in the faraday cage assembly. As a first approximation, we summed simulated TOF curves over all possible ion flight paths originating from a line source. The comparison of measured and simulated TOF distribution is given in Figure S 7.

To subtract the thermal background from experimental data, the modeled TOF distribution of thermal background was included in the fitting procedure, described in Section S.2.2, with the amplitude as a fitting parameter. Due to the tail to very long TOF of the thermal background, this procedure allowed us to distinguish the slow channel and the thermal background. Thermal background was significant only for molecules in the vibrational ground state and in rotational states J<7.

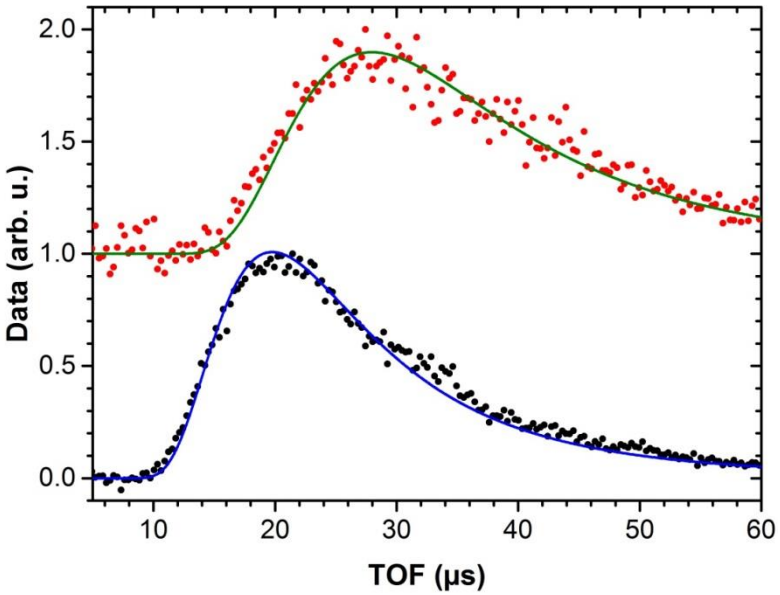

Figure S 7: TOF distributions of thermal background gas, measured for D_2 (red dots) and H_2 (black dots) by leaking gas into the detection chamber. The model described in the text is shown as lines (blue and green). This background contribution is only found for molecules being in low rotational states ($J < 7$) of $v = 0$.

S.3. Tables of parameters obtained from fitting

All reaction probability function parameters are reported in Table S 1-Table S 11. Results are given separated for experimental runs based on the two calibration methods. The given uncertainties are derived from the fitting procedure and represent the standard error, 1σ. Also given are the energy ranges where the experimental data had sufficient signal to noise ratio to describe the sticking probability. As criterion for this, the desorption flux had to be higher than 5% of the maximum. For several quantum states the slow channel could not be characterized due to too low signal caused by the cutoff in the faraday cage assembly. The samples surface temperature was always (923±3) K, except when indicated otherwise. For the five data sets where the temperature was up to 11 K higher exemplary measurements at 923 K showed no distinguishable differences in the results.

Table S 1: Resulting width-parameters for H_2 and both crystal surfaces, given in eV. These values were determined by a global fit, where the data for every rotational state in the corresponding vibrational state was included. This fit was tailored to obtain a single value for $W(\boldsymbol{v})$ but individual results for all other parameters and each J state. Results are presented for datasets from both calibration methods.

H_2	Cu(111)				Cu(211)			
	Knudsen calibration		Internal calibration		Knudsen calibration		Internal calibration	
	value	uncertainty	value	uncertainty	value	uncertainty	value	uncertainty
v = 0	0.189	0.003	0.190	0.002	0.220	0.002	0.220	0.003
v = 1	0.164	0.004	0.169	0.008	0.210	0.003	0.233	0.002

Table S 2: Resulting width-parameters for H_2 and both crystal surfaces, given in eV. These values were determined by a global fit, where the data for every rotational state in the corresponding vibrational state was included. This fit was tailored to obtain a single value for $W(\boldsymbol{v})$ but individual results for all other parameters and each J state. Only datasets using the Knudsen calibration method are available.

HD	Cu(111)		Cu(211)	
	value	uncertainty	value	uncertainty
v = 0	0.188	0.003	0.223	0.002
v = 1	0.161	0.003	0.206	0.003

Table S 3: Resulting width-parameters for D_2 and both crystal surfaces, given in eV. These values were determined by a global fit, where the data for every rotational state in the corresponding vibrational state was included. This fit was tailored to obtain a single value for $W(\boldsymbol{v})$ but individual results for all other parameters and each J state. Results are presented for datasets from both calibration methods.

D_2	Cu(111)				Cu(211)			
	Knudsen calibration		Internal calibration		Knudsen calibration		Internal calibration	
	value	uncertainty	value	uncertainty	value	uncertainty	value	uncertainty
v=0	0.200	0.002	0.190	0.005	0.221	0.002	0.207	0.004
v=1	0.177	0.002	0.165	0.003	0.200	0.002	0.201	0.003
v=2	0.160	0.005	0.140	0.019	0.193	0.003	0.214	0.020

Table S 4: Parameters obtained from the fitting procedure for H_2/Cu(111) and the indicated quantum states, from the dataset relying on the Knudsen calibration method. The energy range where the sticking probability is supported by the experimental data is also indicated.

Cu(111) H_2, v=0	$E_0(v,J)$ / eV		$A_{slow}(v,J)$		$\gamma_{slow}(v,J)$ / eV		Energy range / eV	
J =	value	uncertainty	value	uncertainty	value	uncertainty	lower	upper
0	0.70813	0.00807	0.00224	0.00037	0.09656	0.01154	0.075	0.949
1	0.72008	0.00820	0.00121	0.00019	0.14011	0.02224	0.075	0.949
2	0.72103	0.00825	0.00079	0.00012	0.25531	0.06900	0.075	0.949
3	0.73709	0.00793	0.00044	0.00006	0.94166	0.82968	0.075	1.015
4	0.72342	0.00778	0.00078	0.00012	0.32382	0.10501	0.075	1.015
5	0.71110	0.00817	0.00071	0.00011	0.34885	0.13331	0.075	0.949
6	0.67132	0.00773	0.00078	0.00014	0.22982	0.08078	0.075	0.949
7	0.62611	0.00781	0.00085	0.00019	0.26478	0.14915	0.075	0.888
8	0.57171	0.00819	0.00190	0.00046	0.36293	0.34079	0.075	0.834
9	0.50938	0.00799	0.00467	0.00169	0.11586	0.06481	0.075	0.784
10	0.47366	0.00810	0.08260	0.03450	0.03246	0.00622	0.075	0.738
11	0.37465	0.00939	0.03741	0.03575	0.04738	0.03807	0.075	0.659
H_2, v=1	$E_0(v,J)$ / eV		$A_{slow}(v,J)$		$\gamma_{slow}(v,J)$ / eV		Energy range / eV	
J =	value	uncertainty	value	uncertainty	value	uncertainty	lower	upper
0	0.34240	0.00469	0.16153	0.03922	0.03899	0.00598	0.075	0.658
1	0.35042	0.00473	0.09242	0.02077	0.05097	0.00930	0.075	0.658
2	0.35437	0.00475	0.06495	0.01462	0.05898	0.01256	0.075	0.658
3	0.36438	0.00504	0.03145	0.00586	0.13622	0.05400	0.075	0.658
4	0.35416	0.00582	0.02904	0.00525	0.28895	0.24498	0.075	0.657
5 [a]	0.34361	0.00630	-	-	-	-	0.075	0.657
6 [a]	0.32037	0.00733	-	-	-	-	0.075	0.622
7 [a]	0.28105	0.00786	-	-	-	-	0.075	0.59

[a] The Parameters for the slow channel could not be obtained for these quantum states.

Table S 5: Parameters obtained from the fitting procedure for HD/Cu(111) and the indicated quantum states, from the dataset relying on the Knudsen calibration method. The energy range where the sticking probability is supported by the experimental data is also indicated.

Cu(111) HD, v=0	$E_0(v,J)$ / eV		$A_{slow}(v,J)$		$\gamma_{slow}(v,J)$ / eV		Energy range / eV	
J =	value	uncertainty	value	uncertainty	value	uncertainty	lower	upper
0	0.73095	0.00717	0.00287	0.00061	0.07439	0.00790	0.1	0.998
1	0.71981	0.00706	0.00165	0.00034	0.11619	0.01844	0.1	0.998
2	0.72021	0.00707	0.00105	0.00022	0.14459	0.02891	0.1	0.998
3	0.71399	0.00706	0.00075	0.00015	0.24939	0.08315	0.1	0.998
4	0.71845	0.00713	0.00065	0.00013	0.37866	0.17812	0.1	0.998
5 [a]	0.71891	0.00728	-	-	-	-	0.1	0.998
6 [a]	0.70373	0.00721	-	-	-	-	0.1	0.998
7 [a]	0.67722	0.00746	-	-	-	-	0.1	0.944
8 [a]	0.64111	0.00763	-	-	-	-	0.1	0.913
9 [a]	0.60293	0.00714	-	-	-	-	0.1	0.867
10	0.56007	0.00691	0.00698	0.00408	0.05191	0.01678	0.1	0.824
HD, v=1	$E_0(v,J)$ / eV		$A_{slow}(v,J)$		$\gamma_{slow}(v,J)$ / eV		Energy range / eV	
J =	value	uncertainty	value	uncertainty	value	uncertainty	lower	upper
0	0.41099	0.00392	0.05863	0.01687	0.05333	0.00922	0.1	0.731
1	0.40670	0.00388	0.04728	0.01357	0.06192	0.01243	0.1	0.731
2	0.39926	0.00398	0.04531	0.01419	0.06260	0.01415	0.1	0.697
3	0.38968	0.00395	0.03023	0.01088	0.07635	0.02505	0.1	0.697
4	0.39080	0.00430	0.01923	0.00563	0.16520	0.09393	0.1	0.697
5 [a]	0.39441	0.00499	-	-	-	-	0.1	0.697
6 [a]	0.36902	0.00578	-	-	-	-	0.1	0.665
7 [a]	0.35297	0.00607	-	-	-	-	0.1	0.665

[a] The Parameters for the slow channel could not be obtained for these quantum states.

Table S 6: Parameters obtained from the fitting procedure for D_2/Cu(111) and the indicated quantum states, from the dataset relying on the Knudsen calibration method. The energy range where the sticking probability is supported by the experimental data is also indicated.

Cu(111) D_2, v=0	$E_0(v,J)$ / eV		$A_{slow}(v,J)$		$\gamma_{slow}(v,J)$ / eV		Energy range / eV	
J =	value	uncertainty	value	uncertainty	value	uncertainty	lower	upper
0	0.74785	0.00589	0.00132	0.00017	0.13004	0.01569	0.075	0.975
1	0.75147	0.00590	0.00133	0.00017	0.12045	0.01353	0.075	0.975
2	0.76115	0.00571	0.00100	0.00013	0.15365	0.02026	0.075	1.023
3	0.77671	0.00582	0.00074	0.00009	0.22626	0.03859	0.075	1.029
4	0.79037	0.00594	0.00063	0.00007	0.24565	0.04273	0.075	1.023
5	0.79858	0.00608	0.00038	0.00004	0.78048	0.39429	0.075	1.023
6	0.79690	0.00605	0.00039	0.00004	0.62263	0.25620	0.075	1.023
7	0.78078	0.00594	0.00041	0.00005	0.63489	0.28872	0.075	1.023
8	0.76192	0.00579	0.00048	0.00006	0.41075	0.13742	0.075	1.023
9	0.72938	0.00581	0.00311	0.00040	0.11326	0.01168	0.075	0.975
10	0.69104	0.00582	0.00426	0.00061	0.09760	0.01083	0.075	0.93
11	0.63867	0.00586	0.01310	0.00209	0.07471	0.00776	0.075	0.881
12	0.60040	0.00656	0.08067	0.01097	0.08697	0.00771	0.075	0.853
13	0.53792	0.00618	0.09191	0.01672	0.06141	0.00666	0.075	0.83
14	0.50073	0.00670	0.04542	0.01018	0.07370	0.01384	0.075	0.779
D_2, v=1	$E_0(v,J)$ / eV		$A_{slow}(v,J)$		$\gamma_{slow}(v,J)$ / eV		Energy range / eV	
J =	value	uncertainty	value	uncertainty	value	uncertainty	lower	upper
0	0.47741	0.00387	0.05991	0.00875	0.05033	0.00431	0.075	0.778
1	0.48351	0.00390	0.03736	0.00537	0.05912	0.00581	0.075	0.778
2	0.49231	0.00394	0.02581	0.00363	0.06644	0.00709	0.075	0.778
3	0.49688	0.00399	0.02016	0.00276	0.07595	0.00887	0.075	0.772
4	0.49732	0.00401	0.01669	0.00225	0.08824	0.01167	0.075	0.772
5	0.49398	0.00399	0.01818	0.00251	0.08186	0.01048	0.075	0.772
6	0.48795	0.00387	0.02494	0.00333	0.08137	0.00979	0.075	0.782
7	0.46229	0.00404	0.02166	0.00355	0.07662	0.01210	0.075	0.74
8	0.44861	0.00419	0.03234	0.00484	0.09160	0.01508	0.075	0.74
9	0.40145	0.00374	0.14701	0.08798	0.01824	0.00372	0.075	0.708
D_2, v=2	$E_0(v,J)$ / eV		$A_{slow}(v,J)$		$\gamma_{slow}(v,J)$ / eV		Energy range / eV	
J =	value	uncertainty	value	uncertainty	value	uncertainty	lower	upper
0	0.22037	0.00532	0.52180	0.18934	0.03841	0.01017	0.075	0.582
1	0.24198	0.00539	0.09687	0.05156	0.05928	0.03979	0.075	0.591
2	0.24323	0.00487	0.21888	0.10326	0.04029	0.01520	0.075	0.582
3	0.26613	0.00487	0.08625	0.03386	0.06589	0.03491	0.075	0.614
4	0.27717	0.00606	0.07358	0.01990	0.11611	0.07498	0.075	0.614
5	0.27681	0.00925	0.06287	0.01359	0.41494	0.86509	0.075	0.591
6 [a]	0.28643	0.00792	-	-			0.075	0.609
7 [a]	0.25739	0.00779	-	-			0.075	0.595
8 [a]	0.24796	0.00582	-	-			0.075	0.595

[a] The Parameters for the slow channel could not be obtained for these quantum states.

Table S 7: Parameters obtained from the fitting procedure for H_2/Cu(211) and the indicated quantum states, from the dataset relying on the Knudsen calibration method. The energy range where the sticking probability is supported by the experimental data is also indicated. For the v=1 data, the criterion was chosen as 10% instead of 5%.

Cu(211) H_2, v=0	$E_0(v,J)$ / eV		$A_{slow}(v,J)$		$\gamma_{slow}(v,J)$ / eV		Energy range / eV	
J =	value	uncertainty	value	uncertainty	value	uncertainty	lower	upper
0	0.78302	0.00496	0.00204	0.00031	0.08920	0.00853	0.1	1.015
1	0.78557	0.00497	0.00101	0.00014	0.17637	0.02861	0.1	1.021
2	0.78754	0.00498	0.00090	0.00013	0.15429	0.02343	0.1	1.03
3	0.79625	0.00507	0.00048	0.00006	0.52939	0.23089	0.1	1.035
4	0.78829	0.00500	0.00047	0.00006	0.35672	0.11938	0.1	1.03
5	0.78262	0.00500	0.00036	0.00005	1.02368	0.98339	0.1	1.021
6 [a]	0.74689	0.00500	-	-	-	-	0.1	0.992
7 [a]	0.70941	0.00509	-	-	-	-	0.1	0.952
8	0.65668	0.00510	0.00153	0.00042	0.14140	0.05385	0.1	0.902
9	0.59242	0.00532	0.00388	0.00149	0.10863	0.04851	0.1	0.85
10	0.54396	0.00527	0.02974	0.01672	0.04234	0.01168	0.1	0.801
11 [a]	0.47711	0.00584	-	-	-	-	0.1	0.756
H_2, v=1	$E_0(v,J)$ / eV		$A_{slow}(v,J)$		$\gamma_{slow}(v,J)$ / eV		Energy range / eV	
J =	value	uncertainty	value	uncertainty	value	uncertainty	lower	upper
0	0.47538	0.00512	0.02672	0.00448	0.07313	0.01299	0.075	0.704
1	0.47894	0.00516	0.02107	0.00358	0.08022	0.01598	0.075	0.704
2	0.48729	0.00526	0.01086	0.00193	0.11224	0.03373	0.075	0.712
3	0.49906	0.00510	0.00745	0.00140	0.11477	0.03787	0.075	0.72
4	0.48532	0.00519	0.00876	0.00203	0.08425	0.02668	0.075	0.712
5	0.48444	0.00518	0.00429	0.00135	0.10014	0.05539	0.075	0.712
6	0.43874	0.00501	0.01678	0.01169	0.03469	0.01603	0.075	0.681
7 [a]	0.42907	0.00516	-	-	-	-	0.075	0.658

[a] The Parameters for the slow channel could not be obtained for these quantum states.

Table S 8: Parameters obtained from the fitting procedure for HD/Cu(211) and the indicated quantum states, from the dataset relying on the Knudsen calibration method. The energy range where the sticking probability is supported by the experimental data is also indicated.

Cu(211) HD, v=0	$E_0(v,J)$ / eV		$A_{slow}(v,J)$		$\gamma_{slow}(v,J)$ / eV		Energy range / eV	
J =	value	uncertainty	value	uncertainty	value	uncertainty	lower	upper
0	0.82005	0.00447	0.00054	0.00007	0.18874	0.02968	0.1	1.051
1	0.81878	0.00446	0.00059	0.00007	0.17056	0.02467	0.1	1.051
2	0.81001	0.00442	0.00048	0.00006	0.20233	0.03705	0.1	1.039
3	0.80814	0.00443	0.00029	0.00004	0.38202	0.13283	0.1	1.039
4	0.80765	0.00444	0.00024	0.00003	0.76770	0.52448	0.1	1.039
5 [a]	0.80045	0.00443	-	-	-	-	0.1	1.039
6 [a]	0.81535	0.00449	-	-	-	-	0.1	1.054
7	0.81195	0.00443	0.00022	0.00003	0.31590	0.09969	0.1	1.042
8 [a]	0.75577	0.00453	-	-	-	-	0.1	0.996
9 [a]	0.70784	0.00468	-	-	-	-	0.1	0.951
10	0.66174	0.00437	0.00183	0.00063	0.07628	0.02129	0.1	0.916
HD, v=1	$E_0(v,J)$ / eV		$A_{slow}(v,J)$		$\gamma_{slow}(v,J)$ / eV		Energy range / eV	
J =	value	uncertainty	value	uncertainty	value	uncertainty	lower	upper
0	0.51557	0.00484	0.01548	0.00383	0.09316	0.02340	0.1	0.809
1	0.52689	0.00475	0.00822	0.00196	0.13896	0.05031	0.1	0.817
2	0.52052	0.00488	0.00645	0.00180	0.14662	0.06831	0.1	0.809
3	0.51826	0.00486	0.00687	0.00205	0.12545	0.05421	0.1	0.809
4 [a]	0.52334	0.00495	-	-	-	-	0.1	0.809
5 [a]	0.51345	0.00494	-	-	-	-	0.1	0.801
6 [a]	0.46327	0.00606	-	-	-	-	0.1	0.762
7 [a]	0.42615	0.00625	-	-	-	-	0.1	0.734

[a] The Parameters for the slow channel could not be obtained for these quantum states.

Table S 9: Parameters obtained from the fitting procedure for D_2/Cu(211) and the indicated quantum states, from the dataset relying on the Knudsen calibration method. The energy range where the sticking probability is supported by the experimental data is also indicated. For the v=0 data, the criterion was chosen as 8% instead of 5%.

Cu(211) D_2, v=0	$E_0(v,J)$ / eV		$A_{slow}(v,J)$		$\gamma_{slow}(v,J)$ / eV		Energy range / eV	
J =	value	uncertainty	value	uncertainty	value	uncertainty	lower	upper
0	0.81410	0.00351	0.00104	0.00010	0.12651	0.01057	0.1	1.016
1	0.81510	0.00351	0.00118	0.00012	0.11671	0.00900	0.1	1.015
2	0.81538	0.00353	0.00075	0.00007	0.16818	0.01792	0.1	1.016
3	0.82680	0.00357	0.00065	0.00006	0.17358	0.01817	0.1	1.025
4	0.83464	0.00363	0.00045	0.00004	0.31652	0.05389	0.1	1.036
5	0.84093	0.00365	0.00041	0.00004	0.27650	0.04144	0.1	1.035
6	0.83347	0.00368	0.00034	0.00003	0.81504	0.34110	0.1	1.036
7	0.82300	0.00362	0.00033	0.00003	0.70205	0.27718	0.1	1.025
8	0.80095	0.00360	0.00060	0.00006	0.22784	0.03511	0.1	1.006
9	0.77221	0.00357	0.00073	0.00009	0.15446	0.02146	0.1	0.975
10	0.72307	0.00368	0.00097	0.00014	0.17926	0.03748	0.1	0.935
11	0.69836	0.00364	0.00154	0.00027	0.10163	0.01687	0.1	0.905
12	0.65182	0.00369	0.00235	0.00051	0.10422	0.02331	0.1	0.868
13	0.62658	0.00377	0.00585	0.00168	0.05807	0.01037	0.1	0.837
14	0.56743	0.00403	0.01279	0.00393	0.06704	0.01502	0.1	0.792
D_2, v=1	$E_0(v,J)$ / eV		$A_{slow}(v,J)$		$\gamma_{slow}(v,J)$ / eV		Energy range / eV	
J =	value	uncertainty	value	uncertainty	value	uncertainty	lower	upper
0	0.52025	0.00370	0.03169	0.00384	0.07180	0.00712	0.075	0.813
1	0.51620	0.00377	0.03050	0.00402	0.06417	0.00650	0.075	0.806
2	0.53308	0.00372	0.01759	0.00219	0.07997	0.00924	0.075	0.817
3	0.52707	0.00367	0.02246	0.00309	0.06112	0.00629	0.075	0.821
4	0.54574	0.00378	0.01190	0.00141	0.09717	0.01265	0.075	0.832
5	0.53934	0.00373	0.01160	0.00156	0.07827	0.01002	0.075	0.829
6	0.53874	0.00374	0.01210	0.00154	0.08820	0.01166	0.075	0.828
7	0.52264	0.00369	0.01131	0.00161	0.08822	0.01397	0.075	0.813
8	0.50664	0.00378	0.00845	0.00141	0.09968	0.02255	0.075	0.799
9 [a]	0.52068	0.00445	-	-	-	-	0.075	0.804
10 [a]	0.44382	0.00532	-	-	-	-	0.075	0.758
D_2, v=2	$E_0(v,J)$ / eV		$A_{slow}(v,J)$		$\gamma_{slow}(v,J)$ / eV		Energy range / eV	
J =	value	uncertainty	value	uncertainty	value	uncertainty	lower	upper
0 [a]	0.29135	0.00463	-	-	-	-	0.075	0.636
1 [a]	0.30971	0.00450	-	-	-	-	0.075	0.641
2 [a]	0.31813	0.00451	-	-	-	-	0.075	0.651
3 [a]	0.32870	0.00441	-	-	-	-	0.075	0.666
4 [a]	0.32822	0.00441	-	-	-	-	0.075	0.666
5 [a]	0.34655	0.00447	-	-	-	-	0.075	0.666
6 [a]	0.33021	0.00442	-	-	-	-	0.075	0.666
7 [a]	0.30627	0.00450	-	-	-	-	0.075	0.651
8 [a]	0.30871	0.00450	-	-	-	-	0.075	0.651

[a] The Parameters for the slow channel could not be obtained for these quantum states.

Table S 10: Parameters obtained from the fitting procedure for H_2, both crystal surfaces and the indicated quantum states from the dataset relying on the internal calibration method. The energy range where the sticking probability is supported by the experimental data is also indicated. For the Cu(211) / v=1 data, the criterion was chosen as 10% instead of 5%.

Cu(111) H_2, v=0	$E_0(v,J)$ / eV		$A_{slow}(v,J)$		$\gamma_{slow}(v,J)$ / eV		Energy range / eV	
J =	value	uncertainty	value	uncertainty	value	uncertainty	lower	upper
1 [a]	0.70192	0.00486	0.00197	0.00017	0.11401	0.00895	0.05	0.973
3 [b]	0.72056	0.00482	0.00101	0.00008	0.17772	0.01954	0.05	0.999
5 [b]	0.70150	0.00481	0.00059	0.00005	0.43254	0.12476	0.05	0.986
7 [c]	0.62239	0.00477	0.00167	0.00018	0.10929	0.01441	0.05	0.9
Cu(211) H_2, v=0	$E_0(v,J)$ / eV		$A_{slow}(v,J)$		$\gamma_{slow}(v,J)$ / eV		Energy range / eV	
J =	value	uncertainty	value	uncertainty	value	uncertainty	lower	upper
1	0.78554	0.00678	0.00167	0.00014	0.12238	0.00989	0.05	1.012
3	0.79162	0.00666	0.00111	0.00009	0.14036	0.01311	0.05	1.026
5	0.76829	0.00656	0.00085	0.00007	0.20722	0.03113	0.05	1.012
7	0.68945	0.00650	0.00188	0.00021	0.09217	0.01099	0.05	0.936
Cu(111) H_2, v=1	$E_0(v,J)$ / eV		$A_{slow}(v,J)$		$\gamma_{slow}(v,J)$ / eV		Energy range / eV	
J =	value	uncertainty	value	uncertainty	value	uncertainty	lower	upper
1	0.36628	0.01036	0.30848	0.04616	0.03506	0.00485	0.05	0.668
3	0.37794	0.01046	0.12048	0.02934	0.03770	0.00670	0.05	0.706
5	0.34823	0.00996	0.11369	0.02967	0.04412	0.01061	0.05	0.683
Cu(211) H_2, v=1	$E_0(v,J)$ / eV		$A_{slow}(v,J)$		$\gamma_{slow}(v,J)$ / eV		Energy range / eV	
J =	value	uncertainty	value	uncertainty	value	uncertainty	lower	upper
1	0.44884	0.02563	0.32980	0.14234	0.03488	0.00939	0.05	0.812
3	0.47194	0.02461	0.10504	0.04733	0.04390	0.01635	0.05	0.885
5	0.45442	0.02390	0.05549	0.03044	0.04695	0.02708	0.05	0.874

[a] Surface temperature was 932 K
[b] Surface temperature was 934 K
[c] Surface temperature was 933 K

Table S 11: Parameters obtained from the fitting procedure for D_2, both crystal surfaces and the indicated quantum states from the dataset relying on the internal calibration method. The energy range where the sticking probability is supported by the experimental data is also indicated.

Cu(111) D_2, v=0	$E_0(v,J)$ / eV		$A_{slow}(v,J)$		$\gamma_{slow}(v,J)$ / eV		Energy range / eV	
J =	value	uncertainty	value	uncertainty	value	uncertainty	lower	upper
0	0.72890	0.01302	0.00740	0.00141	0.06941	0.00673	0.05	0.889
2	0.76201	0.01272	0.00382	0.00073	0.06273	0.00551	0.05	0.97
4	0.76888	0.01193	0.00152	0.00028	0.10653	0.01401	0.05	1.035
6	0.76659	0.01136	0.00088	0.00015	0.21463	0.05175	0.05	1.038
Cu(211) D_2, v=0	$E_0(v,J)$ / eV		$A_{slow}(v,J)$		$\gamma_{slow}(v,J)$ / eV		Energy range / eV	
J =	value	uncertainty	value	uncertainty	value	uncertainty	lower	upper
0	0.78839	0.01116	0.00623	0.00103	0.05522	0.00388	0.05	0.963
2	0.80739	0.01064	0.00234	0.00038	0.06351	0.00507	0.05	1.055
4	0.81668	0.01025	0.00078	0.00012	0.12836	0.01750	0.05	1.086
6	0.81766	0.01020	0.00070	0.00010	0.15787	0.02526	0.05	1.078
Cu(111) D_2, v=1	$E_0(v,J)$ / eV		$A_{slow}(v,J)$		$\gamma_{slow}(v,J)$ / eV		Energy range / eV	
J =	value	uncertainty	value	uncertainty	value	uncertainty	lower	upper
0	0.45458	0.00632	0.13211	0.02185	0.04442	0.00404	0.05	0.776
2	0.47238	0.00647	0.05466	0.00856	0.06297	0.00717	0.05	0.782
4 [a]	0.48949	0.00638	0.04355	0.00655	0.06802	0.00758	0.05	0.8
Cu(211) D_2, v=1	$E_0(v,J)$ / eV		$A_{slow}(v,J)$		$\gamma_{slow}(v,J)$ / eV		Energy range / eV	
J =	value	uncertainty	value	uncertainty	value	uncertainty	lower	upper
0	0.51459	0.00505	0.04720	0.00480	0.05198	0.00388	0.05	0.816
2	0.53141	0.00515	0.02592	0.00253	0.06638	0.00578	0.05	0.826
4	0.55135	0.00530	0.01331	0.00126	0.08383	0.00869	0.05	0.835
Cu(111) D_2, v=2	$E_0(v,J)$ / eV		$A_{slow}(v,J)$		$\gamma_{slow}(v,J)$ / eV		Energy range / eV	
J =	value	uncertainty	value	uncertainty	value	uncertainty	lower	upper
2	0.25913	0.01566	0.72995	0.36420	0.02487	0.00801	0.05	0.614
4	0.27080	0.01587	0.51602	0.23422	0.03019	0.01008	0.05	0.629
6	0.27911	0.01619	0.58694	0.25872	0.02840	0.00843	0.05	0.628
Cu(211) D_2, v=2	$E_0(v,J)$ / eV		$A_{slow}(v,J)$		$\gamma_{slow}(v,J)$ / eV		Energy range / eV	
J =	value	uncertainty	value	uncertainty	value	uncertainty	lower	upper
2	0.32203	0.02064	0.35377	0.13663	0.03717	0.01299	0.05	0.647
4	0.33282	0.02116	0.23785	0.09485	0.04003	0.01602	0.05	0.659
6	0.35191	0.02171	0.38398	0.13704	0.03408	0.00945	0.05	0.664

[a] Surface temperature was 927 K

S.4. Angular Distributions

Angular distributions were measured by variation of the polar angle of the sample around the surface normal and integrating the flux of both reaction channels. Signals of five systems have been sampled, all calibrated with the Knudsen cell method. Studied were D_2 (v=0, J=2) and HD (v=0, J=3) from the Cu(111) sample, as well as H_2 (v=0, J=1), D_2 (v=0, J=2) and D_2 (v=1, J=2) from the Cu(211) sample. Unfortunately, the sample mount did not allow for in-situ correction of the alignment of the azimuthal angle. Rather than aligning the Cu(211) surface such that the $(01\bar{1})$-direction was parallel to the sample rotation axis (cf. Figure 2, panels (c+d)), we yielded a deviation of $7° \pm 2°$ relative to that. This orientation of the Cu(211) sample's $(01\bar{1})$-direction almost parallel to the rotation axis was intended to test if the maximum flux was off-normal, e.g. normal to the (111)-terraces, which would result in θ_0 deviating by -19.5° (cf. Figure 2). For the Cu(111) surface, the azimuthal angle was not of interest.

Acquired TOF distributions were analyzed by integrating the flux of each reaction channel as function of the polar angle, $I(\theta)$. These angle-dependent fluxes were then fitted with[8, 9]:

$$I(\theta) = A \times \cos(\theta - \theta_0)^n. \quad \text{(S 3)}$$

This model includes an amplitude factor A, an offset for the center angle θ_0, and the power of the function, n. For the fast desorption channel a highly directed flux distribution ($n \gg 1$) is expected, due to the activation barrier[8, 9]. Because the reactivity of the slow channel decreases with kinetic energy, ($n < 1$) is expected.

All results are summarized in Table S 12, and Figure S 8 shows the distributions from two systems in polar plots. Here, black (fast) and blue (slow) points, respectively show the integrated fluxes of both channels. Red lines show the fitted model of the fast channel and blue lines cosine distributions for comparison. Generally, the angular distributions obtained for the fast channel show strongly peaked behavior with $n \cong 7 - 9$, while the slow channel is best described by significantly broader ($n \leq 4$) distributions.

In panel (Figure S 8a), the flux of both channels is shown on the same scale to illustrate their relative amplitude. Clearly, the acquisition of TOF distributions in the direction normal to the surface discriminates against the detection of the slow channel. For angles away from the surface normal, the slow channel would be detectable with reduced interference of the fast channel.

Table S 12: Fitted $\boldsymbol{n}$ parameters according to Eq. **(S 3)**.

Surface	Isotopologue and quantum state	Channel	$\boldsymbol{n}$
Cu(211)	H_2 (v=0, J=1)	Fast	7.6 ± 0.5
		Slow	0.8 ± 0.4
Cu(211)	D_2 (v=0, J=2)	Fast	9.1 ± 1.5
		Slow	0.4 ± 2.6
Cu(211)	D_2 (v=1, J=2)	Fast	5.9 ± 0.9
		Slow	4.0 ± 0.7
Cu(111)	D_2 (v=0, J=2)	Fast	9.2 ± 0.5
		Slow	1.7 ± 0.5
Cu(111)	HD (v=0, J=3)	Fast	8.6 ± 0.8
		Slow	2.9 ± 0.9

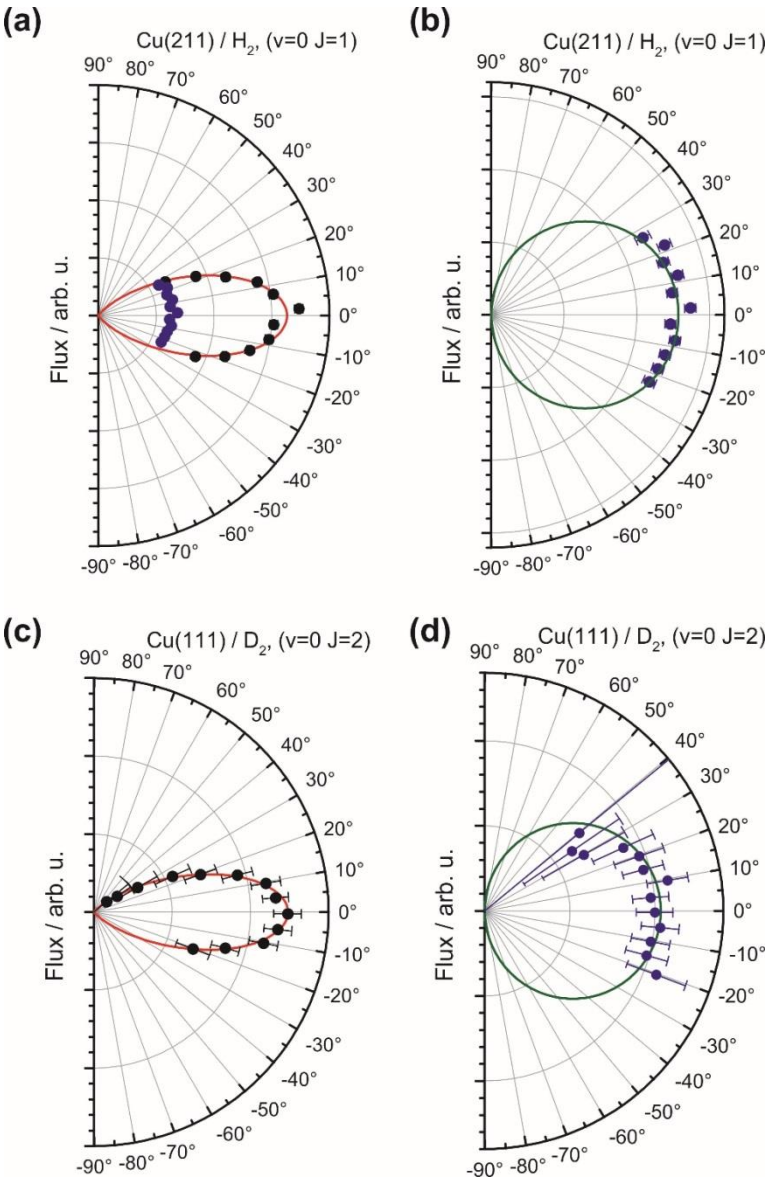

Figure S 8: Illustrative angular distributions measured from both copper facets. Panels (a and b) show data obtained for H_2 (v=0, J=1)/Cu(211) and panels (c and d) for D_2 (v=0, J=2)/Cu(111). In panel (a), the fluxes of both channels are given on the same scale to illustrate their relative amplitudes. In all graphs, the integrated fast channel flux is indicated by black points and the corresponding model as red line. Blue points indicate the integrated flux of the slow channel and green lines show a cosine distribution for comparison.

S.5. Threshold offsets

As elaborated in Section 3.5, are threshold offset values determined from the numerically derived reaction probability curves. In Figure S 9, the methodology is illustrated graphically on a few data sets (filled red symbols) for Cu(111) and Cu(211) in panels (a) and (b). In each subpanel (i) the shown data sets were cut to present only points with amplitudes >25% relative to the fast peak in the flux distribution, thus neglecting the slow channel and thermal background. In the subpanels (ii), the open red symbols show the shifted curves, illustrating that this method considers the whole reaction probability curves instead of only one parameter.

All obtained threshold offsets, as described in Section 3.5 and shown in Figure 9, are reported in Tables S 13-S 15. Uncertainties of these values are best represented by the bin width of 25 meV.

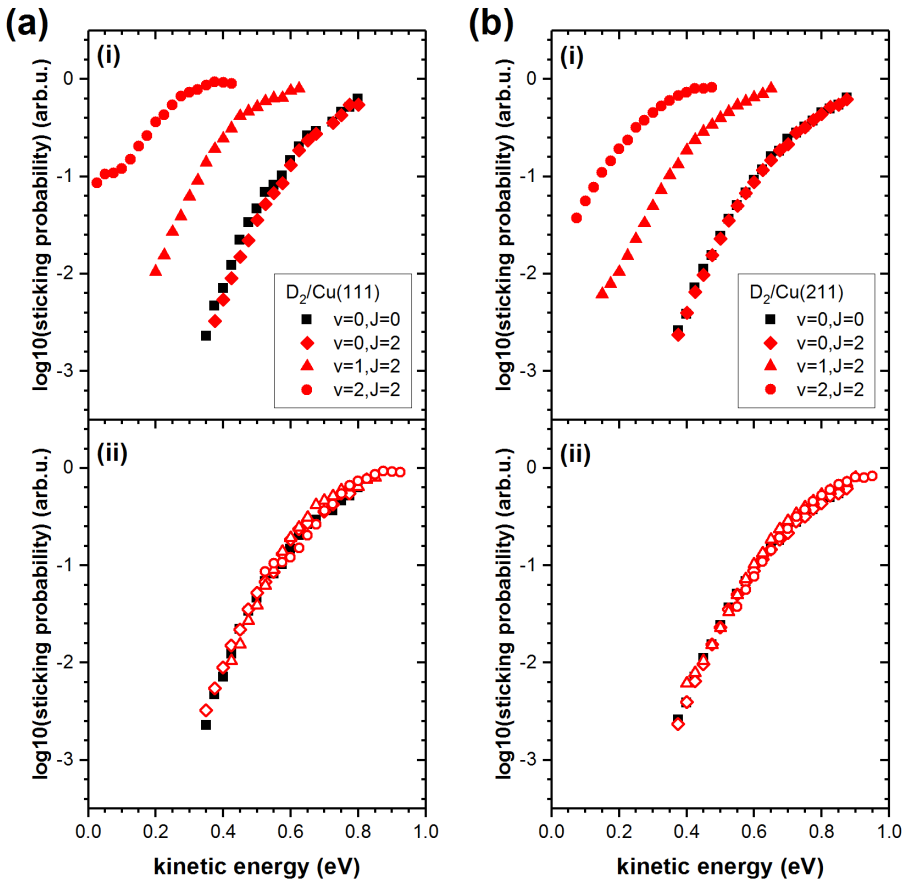

Figure S 9: Determining the threshold offset for several ro-vibrational states. Presented is data from Cu(111) (panel a) and Cu(211) (panel (b), each showing the states D_2, (v=0, J=0, black) and (v=0-2, J=2, red). The upper panels (i) show the scaled sticking probabilities obtained from the TOF curves as described in the text. The lower panels (ii) show the results of shifting these curves in energy to best match with the reference state (open symbols).

Table S 13: Threshold offset values given in Figure 9 for D_2.

D_2	Cu(111)			Cu(211)		
J=	ΔS (v=0) / eV	ΔS (v=1) / eV	ΔS (v=2) / eV	ΔS (v=0) / eV	ΔS (v=1) / eV	ΔS (v=2) / eV
0	0	0.25	0.55	0	0.275	0.5
1	0	0.225	0.5	0	0.275	0.475
2	-0.025	0.225	0.5	0	0.25	0.475
3	-0.025	0.225	0.45	-0.025	0.25	0.45
4	-0.05	0.225	0.45	-0.025	0.25	0.45
5	-0.05	0.225	0.5	-0.025	0.25	0.45
6	-0.05	0.225	0.5	-0.025	0.25	0.45
7	-0.025	0.25	0.5	0	0.275	0.475
8	-0.025	0.275	0.5	0	0.275	0.475
9	0.025	0.325	-	0.05	0.275	-
10	0.05	-	-	0.1	0.35	-
11	0.1	-	-	0.125	-	-
12	0.15	-	-	0.15	-	-
13	0.2	-	-	0.175	-	-
14	0.25	-	-	0.25	-	-

Table S 14: Threshold offset values given in Figure 9 for H_2.

H_2	Cu(111)		Cu(211)	
J=	ΔS (v=0) / eV	ΔS (v=1) / eV	ΔS (v=0) / eV	ΔS (v=1) / eV
0	0	0.325	0	0.3
1	0	0.325	0	0.3
2	-0.025	0.325	0	0.275
3	-0.025	0.35	-0.025	0.275
4	-0.025	0.35	0	0.275
5	0	0.375	0	0.3
6	0.025	0.4	0.025	0.325
7	0.075	0.45	0.075	0.35
8	0.125	-	0.125	-
9	0.2	-	0.2	-
10	0.225	-	0.25	-
11	0.325	-	0.3	-

Table S 15: Threshold offset values given in Figure 9 for HD.

HD	Cu(111)		Cu(211)	
J=	$\Delta \boldsymbol{S}$ (v=0) / eV	$\Delta \boldsymbol{S}$ (v=1) / eV	$\Delta \boldsymbol{S}$ (v=0) / eV	$\Delta \boldsymbol{S}$ (v=1) / eV
0	0	0.3	0	0.275
1	0	0.3	0	0.275
2	0	0.3	0	0.275
3	0.025	0.325	0	0.275
4	0	0.35	0.025	0.275
5	0	0.35	0.025	0.3
6	0.025	0.375	0	0.35
7	0.05	0.4	0	0.375
8	0.1	-	0.075	-
9	0.125	-	0.1	-
10	0.175	-	0.15	-

S.6. Temperature dependent measurements

Figure S 10 presents the results for dependence on surface temperature, acquired for H_2 (v=1, J=1) from Cu(211), which showed the best signal to noise for the slow channel. The TOF distribution was, already presented in Figure S 5. While for γ (Figure S 10 panel (b)) a slight increase with rising temperatures was observed, the relative flux (panel (a)) is not affected significantly. The temperature range could not be extended further in the current setup, since the permeation flux was too low at even lower temperatures. Increasing the temperature above this range resulted in rapid degradation of the faraday cage assembly conditions by the excess thermal radiation of the sample heater.

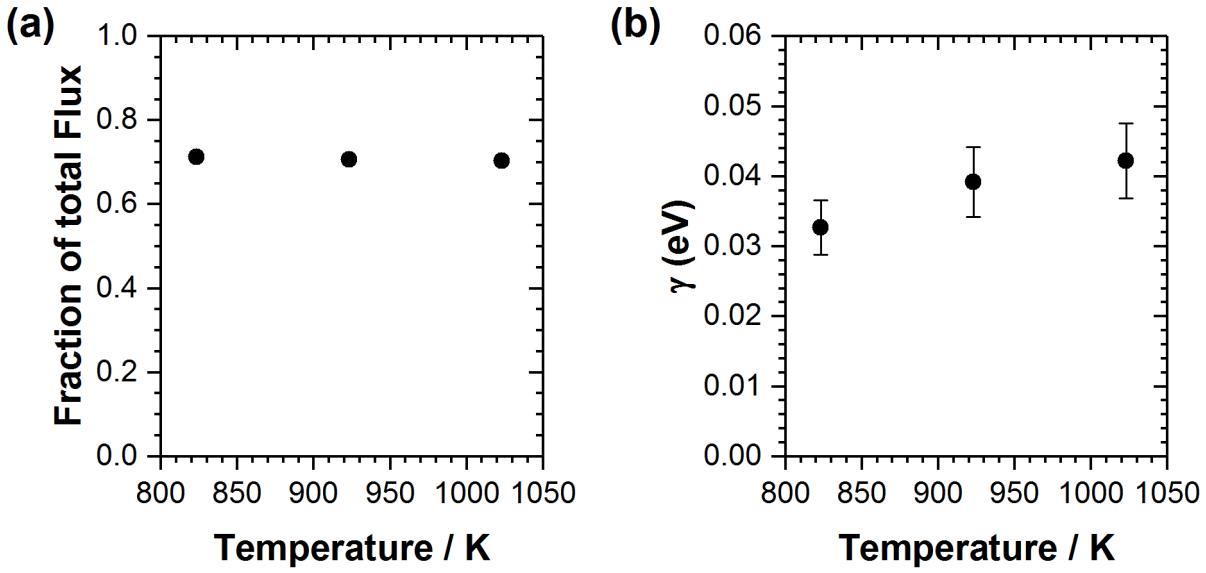

Figure S 10: Temperature dependence of the slow channel parameters, as obtained for the state with best signal to noise ratio: H_2 (v=1, J=1) from Cu(211). Panel (a) shows the fraction of total flux for the slow reaction channel; panel (b) the $\boldsymbol{\gamma}$-parameter. While the $\boldsymbol{\gamma}$- parameterincreases slightly with rising temperatures is the branching ratio of both channels not affected significantly.

S.7. Determination of absolute saturation parameters

The method described in Section 3.6 to obtain absolute saturation values for desorption experiments has been applied previously in other studies, where it was described in detail[4, 10, 11]. Here, only the main aspects of the model will be mentioned briefly. In addition to Equation (11), some assumptions are necessary for this model, the most prominent one being normal energy scaling for the sticking of the molecular beam. Then the width-parameters of the error function (Eq. (5)) that were determined from desorption data was allowed to scale to account for the low surface temperature (120 K) of sticking experiments[4, 10, 11]. Similar as those previous studies we obtain a reduction of the width parameters relative to the values determined at 923 K. For both datasets (D_2 and H_2) we assumed the respective relative saturation values as constant for all quantum states. We fit the model to obtain the absolute scaling of the saturation value and the scaling factor of the widths of the reaction probability curves.

As described by Nattino *et al.*[4], the Cu(111) adsorption data[10, 11] was fitted in two stages. The first residual between model and experiment to be minimized by the fit was defined as $R = \log_{10}(S_{\mathrm{exp}}) - \log_{10}(S_{\mathrm{model}})$, to account for the several orders of magnitude in the measured sticking probabilities. In

the second stage, to be more sensitive for the absolute saturation value, the width-scaling factor was fixed to the previous result and only the saturation value was re-fitted by defining the residual to be minimized as $R = S_{\mathrm{exp}} - S_{\mathrm{model}}$. For our results we also chose to *neglect any contribution from the slow channel*, Eq.(6). This choice was made due to the undetermined temperature dependence for this channel, which would be necessary to extrapolate the contribution at 120 K.

As described by Rettner *et al.*[10], for the H_2 data set the error function parameters (Eq. (5)) for a (v=2)-contribution are necessary for the model. Since those were not measured, we decided to simply extrapolate the $W(v)$ parameter linearly from the results of v=0, 1 and obtained $W(v = 2) = 0.14258$ eV. For the $E_0(v, J)$ parameters, we extrapolated the results from $E_0(v = 0, J)$ by using the vibrational efficacy of 0.63, see Table 1. We included contributions for v=2, J=0-7 in the model.

The results of the model fits are shown in Figures S11 and S12 for H_2 and D_2, respectively. For H_2, the width-parameters resulted as scaled to 69% of the initial values and the absolute sticking probability was determined as A=0.325. For D_2, the absolute sticking probability for all quantum states was determined as A=0.513 and the width-parameters were scaled to 64% of their initial values. In comparison with the literature results[4, 10] the width-scaling is similar while the obtained saturation values are larger. This result was expected from the observed differences in the E_0 parameters, which were discussed in Section 5.1 and the correlation of error function parameters[10, 12, 13].

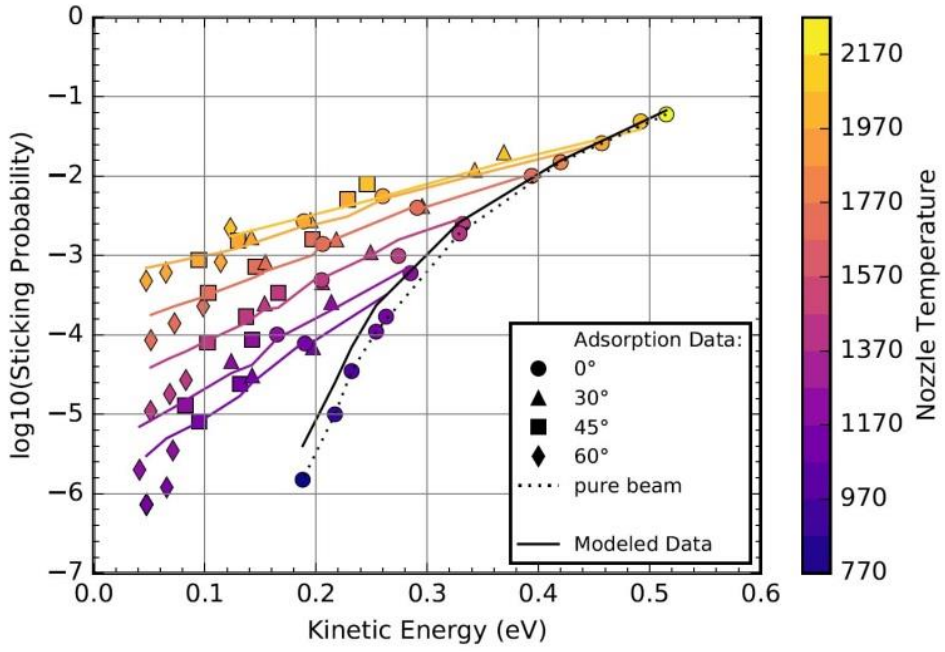

Figure S 11: Result of modeling (straight lines) measured absolute sticking probabilities (symbols) for H_2 obtained in molecular beam adsorption experiments[10]. Here, the widths of the error function curves were scaled to 69% of the values determined by desorption and the absolute saturation values for all quantum states was determined as A = 0.325.

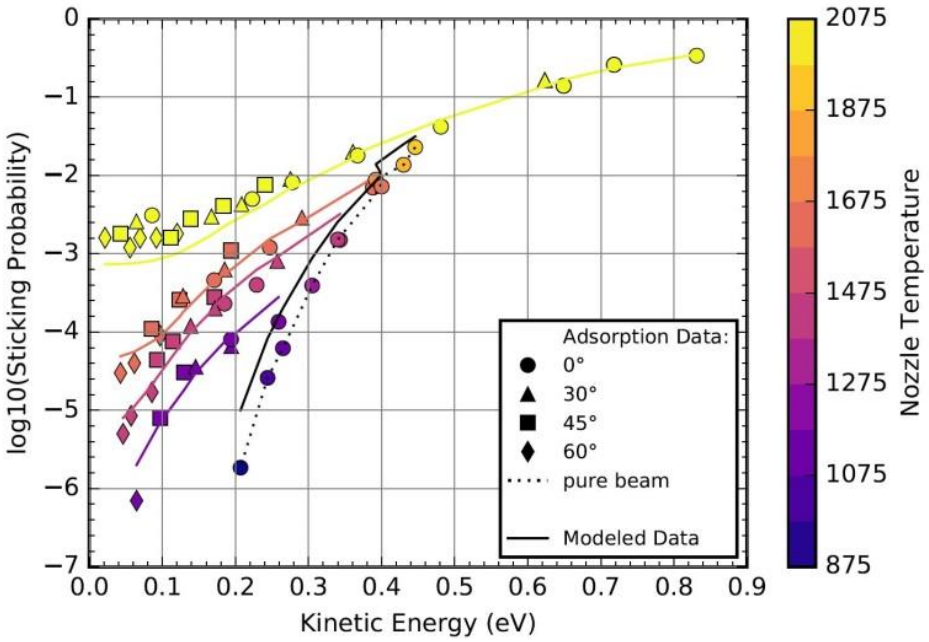

Figure S 12: Result of modeling (straight lines) measured absolute sticking probabilities (symbols) for D2 obtained in molecular beam adsorption experiments[11]. Here, the widths of the error function curves were scaled to 64% of the values determined by desorption and the absolute saturation values for all quantum states was determined as A = 0.513.

References

[1] A. E. Pomerantz *et al.*, Canadian Journal of Chemistry **82** (2004) 723.
[2] H. A. Michelsen, and D. J. Auerbach, The Journal of Chemical Physics **94** (1991) 7502.
[3] H. A. Michelsen *et al.*, The Journal of Chemical Physics **98** (1993) 8294.
[4] F. Nattino *et al.*, Journal of Chemical Physics **141** (2014) 124705.
[5] K. Levenberg, The Quarterly of Applied Mathematics (1944) 164.
[6] D. Marquardt, Journal of the Society for Industrial and Applied Mathematics **11** (1963) 431.
[7] M. Newville, Stensitzki, T., Allen, D. B., Ingargiola, A., 2014).
[8] W. Van Willigen, Physics Letters A **28** (1968) 80.
[9] G. Anger, A. Winkler, and K. D. Rendulic, Surface Science **220** (1989) 1.
[10] C. T. Rettner, H. A. Michelsen, and D. J. Auerbach, The Journal of Chemical Physics **102** (1995) 4625.
[11] C. T. Rettner, D. J. Auerbach, and H. A. Michelsen, Physical Review Letters **68** (1992) 1164.
[12] M. J. Murphy, and A. Hodgson, The Journal of Chemical Physics **108** (1998) 4199.
[13] M. Wijzenbroek, and M. F. Somers, The Journal of chemical physics **137** (2012) 054703.